

MRISegmentator-Abdomen: A Fully Automated Multi-Organ and Structure Segmentation Tool for T1-weighted Abdominal MRI

Yan Zhuang^{1*}, Tejas Sudharshan Mathai^{1†}, Pritam Mukherjee^{1†},
Brandon Khoury², Boah Kim¹, Benjamin Hou¹, Nusrat Rabbee³,
Ronald M. Summers¹

^{1*}Radiology and Imaging Sciences, National Institutes of Health Clinical Center, 10 Center Dr, Bethesda, 20892, MD, USA.

²Department of Radiology, Walter Reed National Military Medical Center, 8901 Rockville Pike, Bethesda, 20892, MD, USA.

³Biostatistics and Clinical Epidemiology Services, National Institutes of Health Clinical Center, 10 Center Dr, Bethesda, 20892, MD, USA.

*Corresponding author(s). E-mail(s): yan.zhuang2@nih.gov;
Contributing authors: tejas.mathai@nih.gov; pritam.mukherjee@nih.gov;
brandon.r.khoury.mil@health.mil; boah.kim@nih.gov;
benjamin.hou@nih.gov; nusrat.rabbee@nih.gov; rsummers@cc.nih.gov;

[†]These authors contributed equally to this work.

Abstract

Background Segmentation of organs and structures in abdominal MRI is useful for many clinical applications, such as disease diagnosis and radiotherapy. Current approaches have focused on delineating a limited set of abdominal structures (13 types). To date, there is no publicly available abdominal MRI dataset with voxel-level annotations of multiple organs and structures. Consequently, a segmentation tool for multi-structure segmentation is also unavailable.

Methods We curated a T1-weighted (T1w) abdominal MRI dataset consisting of 195 patients who underwent imaging at National Institutes of Health (NIH) Clinical Center. The dataset comprises of axial pre-contrast T1, arterial, venous, and delayed phases for each patient, thereby amounting to a total of 780 series (69,248 2D slices). Each series contains voxel-level annotations of 62 abdominal organs and structures. A 3D segmentation (nnUnet) model, dubbed as MRISegmentator-Abdomen (MRISegmentator in short), was trained on this

dataset, and evaluation was conducted on an internal test set and two large external datasets: AMOS22 and Duke Liver. The predicted segmentations were compared against the ground-truth using the Dice Similarity Coefficient (DSC) and Normalized Surface Distance (NSD).

Findings MRISegmentator achieved an average DSC of 0.861 ± 0.170 and a NSD of 0.924 ± 0.163 in the internal test set. On the AMOS22 dataset, MRISegmentator attained an average DSC of 0.829 ± 0.133 and a NSD of 0.908 ± 0.067 . For the Duke Liver dataset, an average DSC of 0.933 ± 0.015 and a NSD of 0.929 ± 0.021 was obtained.

Interpretation The proposed MRISegmentator provides automatic, accurate, and robust segmentations of 62 organs and structures in T1-weighted abdominal MRI sequences. The tool has the potential to accelerate research on various clinical topics, such as abnormality detection, radiotherapy, disease classification among others. We make the dataset and segmentation model publicly available.

Funding This work was supported by the Intramural Research Program of the National Institutes of Health (NIH) Clinical Center (project number 1Z01CL040004)

Keywords: Multi-organ, Multi-structure, Segmentation, MRI, Abdomen, T1w

1 Introduction

Magnetic Resonance Imaging (MRI) is a fundamental and versatile tool in medical imaging, and it is widely incorporated into clinical workflows (Dirix et al (2014)) due to its comprehensive diagnostic capabilities. Automating the delineation of organs and structures on MRI sequences can enable downstream applications, such as the early detection of cancer (Mathai et al (2024)), tracking interval changes in size of radiologic findings, the diagnosis of diffuse and focal liver disease (Macdonald et al (2023)), radiotherapy planning and guidance (Keall et al (2022)), and quantification of body composition for opportunistic screening of diseases (Zaffina et al (2022)). Auto-segmentation of multiple structures can improve patient outcomes without increasing the burden on radiologists (Zhu et al (2023)).

Numerous studies have explored MRI segmentation across various body parts, such as the brain, heart, abdomen, and pelvis (Billot et al (2023); Zhuang et al (2019); Macdonald et al (2023); Nyholm et al (2018)). Despite recent advancements, these works focus on a limited set of organs and structures. In particular, multi-organ and structure segmentation for abdominal MRI lags significantly behind its CT counterpart. Furthermore, the process of annotating multiple organs and structures in radiologic studies is not only time-consuming and labor-intensive, but often requires medical expertise that can make the annotation process prohibitively expensive (Greenspan et al (2016)). This challenge is amplified in the case of the abdomen, which is an anatomically complex area with several subtle structures. As a result, there is a noticeable lack of large-scale, high-quality MRI datasets with voxel-level annotation, detailed information on MRI acquisition, and transparent data on patient demographics.

Presently, the AMOS22 dataset (Ji et al (2022)) stands as the largest abdominal MRI dataset that is publicly available to the best of our knowledge. However, annotations were only provided for 13 key abdominal organs across 60 patients, and comprehensive data acquisition and patient demographics information were not available. Meanwhile, the Duke Liver MRI dataset, which was recently released, restricted the annotations provided solely to the liver (Macdonald et al (2023)). In contrast, there are several publicly available abdominal CT datasets (Ma et al (2022)) that contain the requisite amount of data for training robust automated tools. These datasets have contributed to the development of a powerful CT-based multi-structure segmentation tool, TotalSegmentator (TS), that can delineate 117 different structures in the body (Wasserthal et al (2023)). It is the current *de-facto* standard for benchmarking multi-organ and structure segmentation tasks in CT. However, such a tool for abdominal MRI does not exist currently, and there is a pressing demand to create a robust and accurate tool for abdominal MRI.

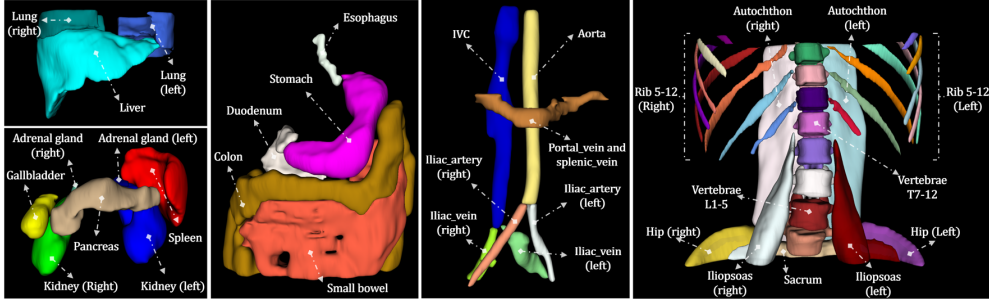


Fig. 1: We developed a multi-organ and structure segmentation tool called MRISegmentator-Abdomen (**MRISegmentator** in short) to segment 62 organs and structures in abdominal T1w MRI studies. The tool comprehensively covers various anatomical regions in the abdomen including 15 major organs, 7 vessels, 8 muscles, and 32 skeletal structures. Visual examples of the segmentations for these organs and structures are shown above.

In this study, we curated a large-scale multi-parametric abdominal T1-weighted (T1w) MRI dataset. The dataset contains 780 volumes, including both pre-contrast T1-weighted (T1w PRE) and contrast-enhanced T1-weighted in the arterial (T1w ART), portal venous (T1w VEN), and delayed (T1w DEL) phases, totalling 69,248 2D slices from 195 unique patients. As shown in Fig. 1, voxel-level annotations for 62 organs and structures across various regions in the abdomen were obtained. The annotation process was comprised of a two-step semi-automated annotation pipeline. First, cross-modality segmentation methods were utilized for producing large-scale pseudo-labels to reduce annotation time. Then, an iterative learning strategy was adopted, in which successive models were trained on refined versions of annotations derived from the outputs of previous models. This led to powerful models being progressively created with improved annotations obtained in each round. Once the annotations were available for all structures in all volumes, the proposed MRISegmentator-Abdomen

(**MRISegmentator** in short) model was developed to segment structures in abdominal T1w MRI. Evaluations on an internal dataset showed that the tool effectively segmented 15 major organs, 7 blood vessels, 8 muscles groups, and 32 bones within the abdomen. Furthermore, external validation on the AMOS22 and Duke Liver datasets corroborated its robustness to studies acquired at external institutions. The dataset and segmentation model are publicly available¹.

2 Materials and Methods

2.1 Patient Sample

This retrospective study utilized three different datasets, one internal and two external, which are described next.

Internal Dataset. The internal dataset was Health Insurance Portability and Accountability Act (HIPAA) compliant and approved by the Institutional Review Board at NIH Clinical Center. The requirement for signed informed consent from the patients was waived. The Picture Archiving and Communication System (PACS) system at the National Institutes of Health Clinical Center (NIH CC) was queried for patients who underwent both abdominal MRI and CT scans on the same day, between January 2019 and October 2021 at the NIH CC (Mathai et al (2023, 2022)). As shown in Fig. 8 in supplementary materials, out of 632 patients who met the search criteria, 225 were randomly selected for the annotation. The patients in the sample had a variety of underlying pathological conditions, such as liver tumors and pancreatic cysts. 30 patients were excluded as they had severe metastatic disease and annotation of all the lesions for these patients would be very cumbersome. As a result, the final patient sample consisted of 195 patients.

Each patient had all four axial T1 images: (1) pre-contrast T1-weighted (T1w PRE), (2) contrast-enhanced T1-weighted in the arterial (T1w ART), (3) portal venous (T1w VEN), and (4) delayed (T1w DEL) phases, respectively. This resulted in a total of 780 MRI images for 195 patients. CT images acquired on the same day for these 195 patients were also collected, and these images contained both contrast and non-contrast images. Table 1 in the supplementary materials summarizes the acquisition parameters and demographic details of the internal dataset. The CT images served as a base to generate pseudo-annotations for the MRI sequences, which will be discussed in Section 2.2. Their acquisition information is shown in Table 3 in the supplementary materials.

External Dataset. The first of two external datasets was a subset of the MRI data released as part of the Multi-Modality Abdominal Multi-Organ Segmentation Challenge 2022 (AMOS22) challenge (Ji et al (2022)). The AMOS22 dataset (MRI subset) contained 60 multi-planar, multi-sequence MRI volumes from 60 patients. It provided segmentation annotations for 13 main abdominal organs, including the kidneys, liver, and stomach, among others. However, it did not provide detailed information related to the sequence type and patient demographics. Thus, the AMOS22 dataset (whole MRI

¹The dataset and segmentation model will be publicly available upon acceptance of the paper.

subset) was employed to evaluate the segmentation performance of MRISegmentator on these 13 major organs.

The second external dataset was the Duke Liver dataset (Macdonald et al (2023)) that contained 2146 multi-parametric MRI series from 105 patients. In contrast to the AMOS22 dataset, it offered comprehensive details on data acquisition and patient demographics. Given that it exclusively contained annotations of the liver, the second external validation study specifically focused on evaluating the performance of MRISegmentator for liver segmentation. As shown in Fig. 9 in the supplementary materials, we excluded MRI volumes that were not T1w MRI series and those volumes that lacked liver segmentation labels, which narrowed the dataset down to 172 T1w MRI volumes from 95 patients. Detailed information on data acquisition and patient demographics information of the Duke Liver dataset used in our study can be found in Table 2 in the supplementary materials. For further information about these two datasets, we refer interested readers to the respective publications (Macdonald et al (2023); Ji et al (2022)).

2.2 Annotation

The internal dataset was annotated to provide segmentation maps of 62 annotated abdominal organs and structures, thereby offering comprehensive coverage across various anatomical regions within the abdomen. These structures were organised into four different categories based on their anatomical locations and physiology: (1) Group 1 (G1) includes 15 major organs, (2) Group 2 (G2) consists of 7 blood vessels, (3) Group 3 (G3) includes 8 muscles, and (4) Group 4 (G4) contains 32 skeletal structures. For a detailed enumeration of the organs and structures within each group, the reader is referred to Section 6.4 in the supplementary materials.

Annotating 62 organs and structures across 780 volumes (equating to 69,248 2D slices) is a task of considerable complexity and an exceedingly labor-intensive endeavor (Park et al (2020)). As shown in Fig. 2, a semi-automated annotation approach was adopted to reduce the time required for annotation. First, the “cross-domain segmentation” step seen in Fig. 2(a) produced preliminary segmentations (also called pseudo-labels). Subsequently, these pseudo-labels were incrementally refined through an iterative learning approach over multiple iterations as shown in Fig. 2(b).

The upper branch of Fig. 2(a) illustrates the process of generating non-musculoskeletal masks for organs and vessels in groups G1 and G2 (*e.g.*, liver and aorta) through synthetic segmentation (Zhuang et al (2024)). This process involved conversion of the MRI volumes into synthetic CT volumes. Subsequently, the CT-based TotalSegmentator (TS) tool (Wasserthal et al (2023)) predicted the corresponding segmentation masks for these synthetic CT volumes. The masks were then mapped back to the MRI volume as pseudo-labels. The bottom branch of Fig. 2(a) depicts the creation of pseudo-masks for muscle and bone structures in G3 and G4 (*e.g.*, spines and gluteus muscles) through the segmentation of paired CT scans. We registered the paired CT and MRI volumes together for each patient, and applied TS to the registered CT volumes to generate pseudo-labels. These pseudo-labels were manually refined by an expert grader (YZ) to ensure they accurately aligned with the

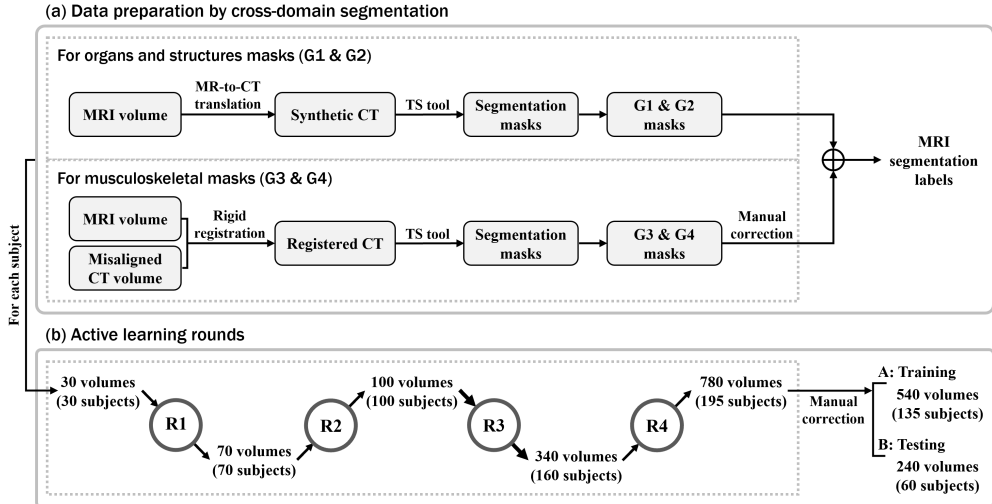


Fig. 2: The semi-automated annotation pipeline consists of two steps: (a) a data preparation step; (b) an iterative learning pipeline. First, the cross-domain segmentation method was leveraged to derive large-scale pseudo-labels. This involved synthetic translation of MRI volumes into CT, pseudo-label generation using TotalSegmentator (TS) for the synthetic CT volumes, and subsequent mapping of pseudo-labels back to the MRI volumes. Then, the iterative learning strategy refined the pseudo-annotations in each round. The upper branch of (a) was used to obtain masks for main abdominal organs and structures in G1 and G2. The bottom branch of (a) was utilized to obtain segmentation masks for musculoskeletal structures in G3 and G4. The iterative learning pipeline included multiple iterations of “training-correction-retraining”. In each iteration, manual refinements of pseudo-labels were incorporated into the training phase to yield a powerful model, which was subsequently used to generate pseudo-labels on additional MRI volumes in the next iteration. At the end of the iterative learning pipeline, the dataset was randomly split into a training set and a testing set.

underlying anatomy. Following this, we combined all pseudo-masks to form the initial segmentation masks, setting the stage for the next round of active learning.

In the second setup, the iterative learning pipeline involved several iterations of “training-refinement-retraining” procedure to incorporate experts’ corrections and to progressively improve the segmentation masks within each round from Round 1 (R1) to Round 4 (R4). For each training round, a grader (YZ) initially refined the initial segmentations manually. Following this, an nnU-Net segmentation network (Isensee et al (2021)) was trained to generate predictions for additional volumes that were utilized in the subsequent rounds. At the end of R4, comprehensive voxel-wise segmentations for each of the 62 structures were obtained for all 780 MRI volumes across 195 patients.

The dataset was then randomly split into training (135 patients, 540 MRI volumes) and testing sets (60 patients, 240 MRI volumes). Within the training set, a radiology resident (BK) verified the annotations for one sequence per patient for a subset of 60 out of the 135 patients. Following this, the grader (YZ) manually corrected the

annotations, and also reviewed and amended the annotations for the rest. In the testing set, both a senior board-certified radiologist with 30+ years of experience (RMS) and a radiology resident (BK) manually reviewed two sequences per patient. The grader (YZ) then manually refined the annotations for all testing set volumes based on their collective feedback.

2.3 Deep Learning Model

MRISegmentator utilized the self-configuring 3D nnUNet segmentation framework (Isensee et al (2021)), which currently stands as the *de-facto* standard in medical image segmentation. The nnUNet model has won multiple challenges with benchmark datasets and been robustly validated in contrast to recent novel CNN-based, transformer-based, and Mamba-based architectures (Isensee et al (2024)). Built on the PyTorch framework, it automatically identified the optimal hyper-parameters for training a segmentation model, enabling it to efficiently segment target structures of interest. Models trained using this framework can be easily shared with the research community for reproducibility. During the training phase, MRISegmentator processed MRI volumes along with the corresponding segmentation masks for 62 distinct structures as input. A 3D full-resolution nnUNet was trained with five-fold cross-validation, and it resulted in five models that were used in an ensemble for prediction on the test set. The number of training epochs was set to 2000 to account for the large number of structures. The loss function was an equally weighted combination of binary cross-entropy and soft Dice losses. Optimization of this loss function was achieved using the Adam optimizer with an initial learning rate of 10^{-2} , a polynomial learning rate scheduler, and a batch size of 2. All experiments were conducted using an NVIDIA A100 80GB GPU on the NIH Biowulf high-performance computing cluster.

3 Experiments and Statistical Analysis

Experiments. The performance of MRISegmentator was assessed through validation on both internal and external test datasets. For the internal test set, segmentation results produced by the proposed tool for all 62 organs and structures were analyzed. External validation of MRISegmentator was conducted on the AMOS22 MRI data subset (60 patients, 60 volumes) and the Duke Liver dataset (95 patients, 172 volumes). Additionally, MRISegmentator’s performance was compared against other state-of-the-art methods on the validation set of the AMOS22 MRI subset (20 patients, 20 volumes), as reported by Ji et al. (Ji et al (2022)). The segmentation accuracy was quantitatively measured using the Dice Similarity Coefficient (DSC) and Normalized Surface Distance (NSD).

An additional experiment was also conducted wherein a 3D full-resolution nnUNet model “nnUNet-AMOS” was trained on the AMOS22 dataset. This model then predicted segmentation masks for 13 structures in the internal dataset. As AMOS22 is currently the largest publicly available MRI dataset with labels for 13 structures, the intent of this experiment was to determine the performance of a model trained on AMOS22 and tested on the internal test dataset. The segmentations from both

“nnUNet-AMOS” and MRISegmentator were compared to evaluate the effectiveness of each model.

Statistical Analysis. For each patient, the DSC and NSD scores were calculated for each of the 62 structures. Two statistical tests were conducted to measure the tool’s performance. First, a two-sided Student’s t-test was performed to compare the DSC scores between MRISegmentator and nnUNet-AMOS. A p-value $< .05$ was considered statistically significant. Second, the performance across different MRI series (e.g., PRE vs. ART vs. VEN vs. DEL) was done to investigate the segmentation consistency across all sequences. To account for the correlations between two series from the same patient, a mixed-effects statistical model was run with the DSC scores as the dependent variable, the MRI sequence type and organ as fixed effects, incorporated a random effect for each patient. Marginal means for each type of sequence (PRE vs. ART vs. VEN vs. DEL) were obtained as well as corresponding standard errors.

4 Results

4.1 Internal Dataset

Fig. 3 shows the mean DSC for the 62 organs and structures across all patients. Tables 4 and 5 in the supplementary materials show the DSC and NSD scores (mean \pm std). Fig. 4 depicts the segmentation results for a patient in the axial, sagittal, and coronal views. The color map of the segmentation mask for each organ is shown Fig. 13 in the supplementary materials.

Overall, MRISegmentator achieved an average DSC of 0.861 ± 0.170 and a NSD of 0.924 ± 0.163 across all 62 organs and structures in the abdomen for all scans in the internal test set. The segmentation results were also analyzed for each group of structures. The DSC and NSD were for G1 (15 major organs) 0.918 ± 0.069 and 0.959 ± 0.067 ; G2 (vessels) 0.913 ± 0.105 and 0.972 ± 0.080 ; G3 (muscles) 0.929 ± 0.093 and 0.971 ± 0.084 ; and G4 (bones) 0.806 ± 0.250 and 0.886 ± 0.245 , respectively.

Larger organs and structures with relatively non-complex anatomical shapes, such as the liver, spleen, kidneys and autochthonous (back) muscles in G1 and G3, achieved the highest DSC scores. Conversely, as anatomical complexity increased, structures like the small bowel, colon, stomach, and pancreas yielded lower DSC scores. The DSC scores were lowest when delineating smaller organs and structures, such as adrenal glands and ribs. There are inherent difficulties in segmenting small objects, and they are further compounded by potential patient movement and imaging artifacts. MRISegmentator encountered challenges while delineating structures located at the transition from the chest to the abdomen, or from the abdomen to the pelvis. For example in Fig. 3, the lowest DSC scores were seen for the thoracic ribs (rib_4 and rib_5) and thoracic vertebrae (T7), which are located at the transitional intersection of the lower chest and upper abdomen.

The DSC scores for the pre-contrast (PRE), arterial (ART), venous (VEN), and delayed (DEL) phases were 0.863 ± 0.231 , 0.874 ± 0.217 , 0.880 ± 0.212 , and 0.876 ± 0.220 , respectively. NSD scores were 0.922 ± 0.208 , 0.932 ± 0.196 , 0.937 ± 0.191 , 0.933 ± 0.197 ,

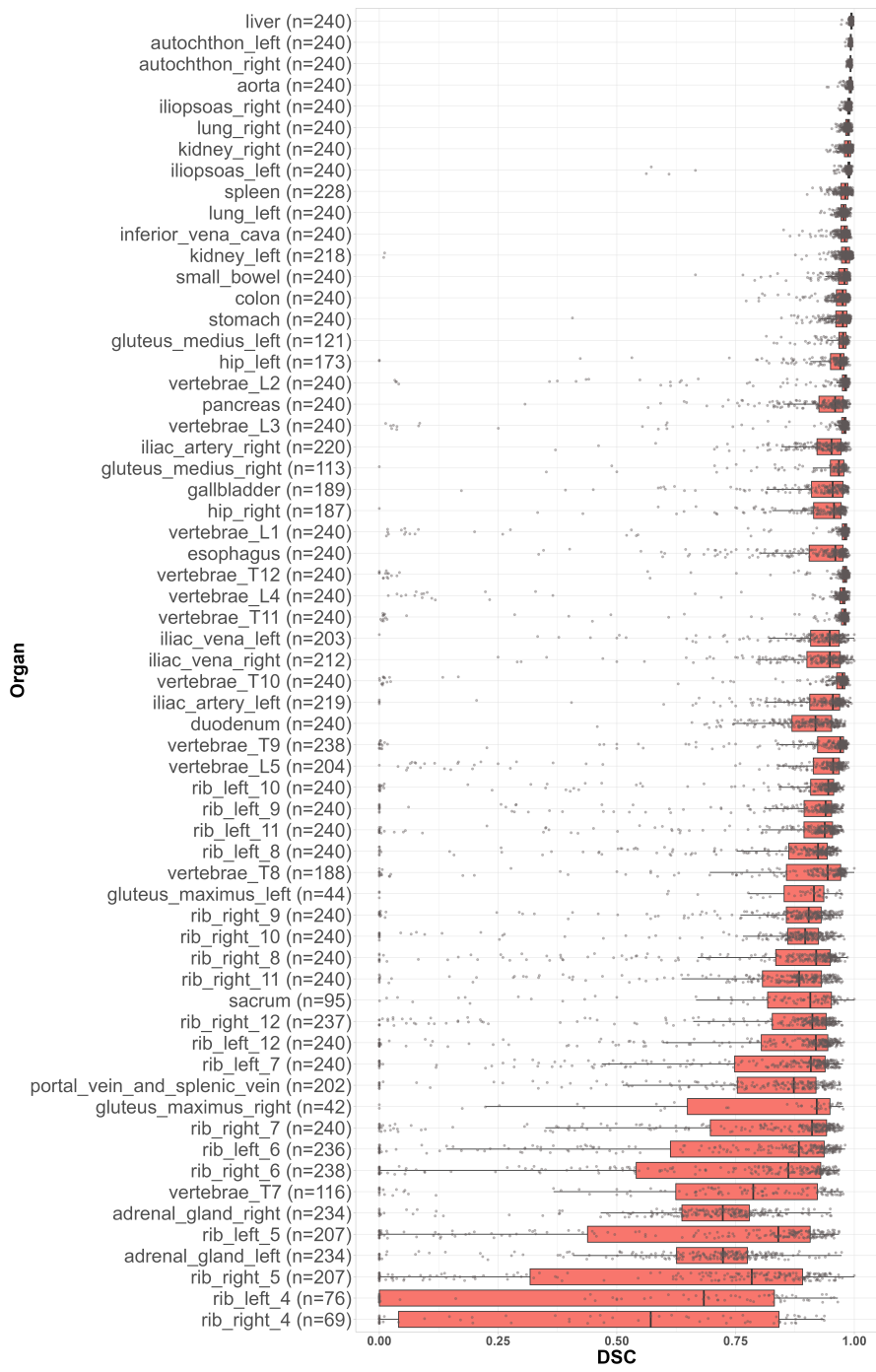


Fig. 3: Dice scores for all 62 organs and structures (ranked descending order of performance). The number of volumes in the training data subset that the structure was present in is also indicated.

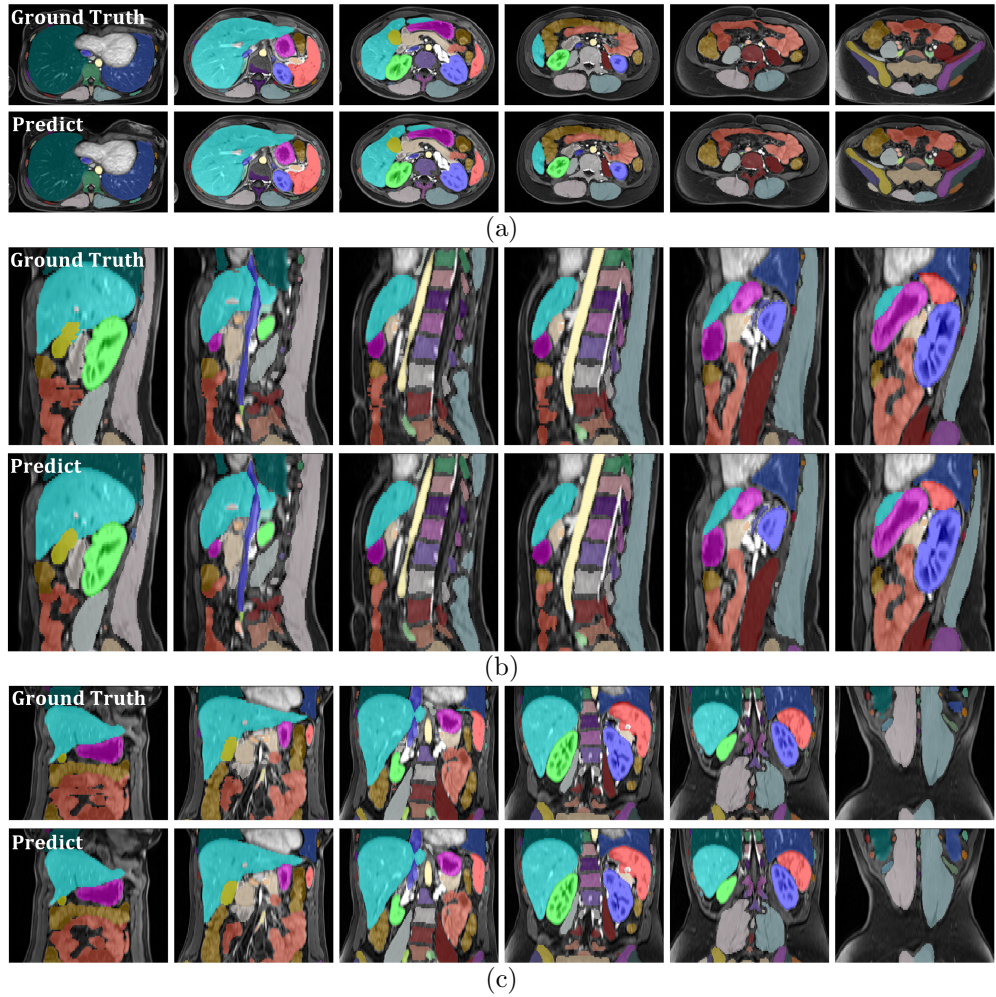


Fig. 4: Ground truth and predicted segmentation results for one patient in axial, sagittal, and coronal views: (a) Axial view - Segmentation results from superior to inferior; (b) Sagittal view - Segmentation results from right to left; (c) Coronal view - Segmentation results from anterior to posterior. The color map of segmentation for each organ is provided in Fig. 13 in the supplementary materials.

respectively. The pre-contrast T1 MRI (PRE) sequence exhibited the lowest performance, primarily due to being a pre-contrast sequence where some organs (pancreas) and structures (vessels) do not show any enhancement patterns, which affects the precise segmentation of these structures. The mixed-effects model analysis found that the differences between PRE and the ART/VEN/DEL sequences were statistically significant ($p < 0.05$), indicating a higher segmentation accuracy in post-contrast phases. However, no significant difference were observed among the ART/VEN/DEL

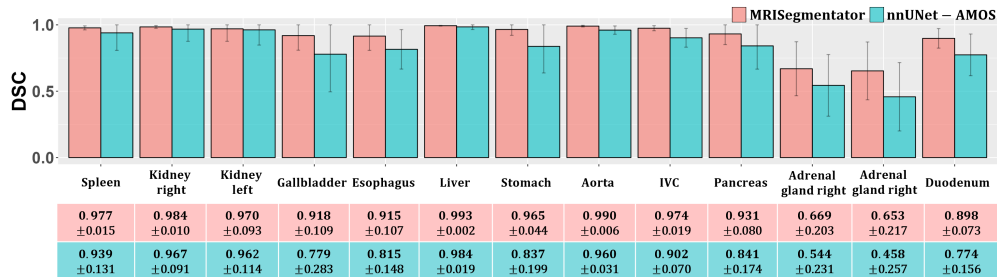


Fig. 5: Comparison of segmentation performance between MRIsegmentator and nnUNet-AMOS for 13 key organs in the internal dataset. These organs were chosen as nnUNet-AMOS was trained on the AMOS22 dataset that contained 13 organ labels.

sequences, which suggested a comparable segmentation performance for these three sequences.

Fig. 5 shows the DSC scores obtained by MRIsegmentator and nnUNet-AMOS for 13 major abdominal organs in the internal dataset. Detailed NSD scores from both MRIsegmentator and nnUNet-AMOS for the 13 structures are provided in Table 6 in the supplementary materials. Again, MRIsegmentator outperformed nnUNet-AMOS by a large margin for a majority of organs, such as the gallbladder, stomach, and duodenum. For large organs, such as the kidneys and the liver, the performance differences were subtle. For DSC scores, MRIsegmentator significantly outperformed nnUNet-AMOS ($p < .0038$, two-sided t-test with Bonferroni correction). One contributing factor to the decreased segmentation performance of nnUNet-AMOS was the presence of a variety of pathological cases in the internal dataset, including liver tumors and pancreatic cysts. The AMOS22 dataset does not contain training data from patients with different pathologies. Fig. 6 presents several instances where nnUNet-AMOS failed to accurately segment regions affected by pathological changes, leading to a decrease in DSC scores in these cases.

4.2 External Dataset

Fig. 7 shows the segmentation performance of MRIsegmentator for each of the 13 organs across all 60 patients in the AMOS22 dataset. Overall, MRIsegmentator achieved an average DSC of 0.829 ± 0.133 across 13 organs. Table 6 in the supplementary materials shows the DSC and NSD scores for each individual organ. On the validation set of the AMOS22 MRI subset (20 patients, 20 volumes), MRIsegmentator obtained a mean DSC of 0.844, which the second-best performance compared to other methods that were directly trained on the AMOS22 dataset (CoTr (Xie et al (2021)): 0.775, nnFormer (Zhou et al (2021)): 0.806, Swin-UNetr (Hatamizadeh et al (2021)): 0.757, UNet (Ronneberger et al (2015)): 0.856, UNetr (Hatamizadeh et al (2022)): 0.753, VNet (Milletari et al (2016)): 0.837), as reported by Ji et al. (Ji et al (2022)). This observation is remarkable as MRIsegmentator was not directly trained with the AMOS22 dataset.

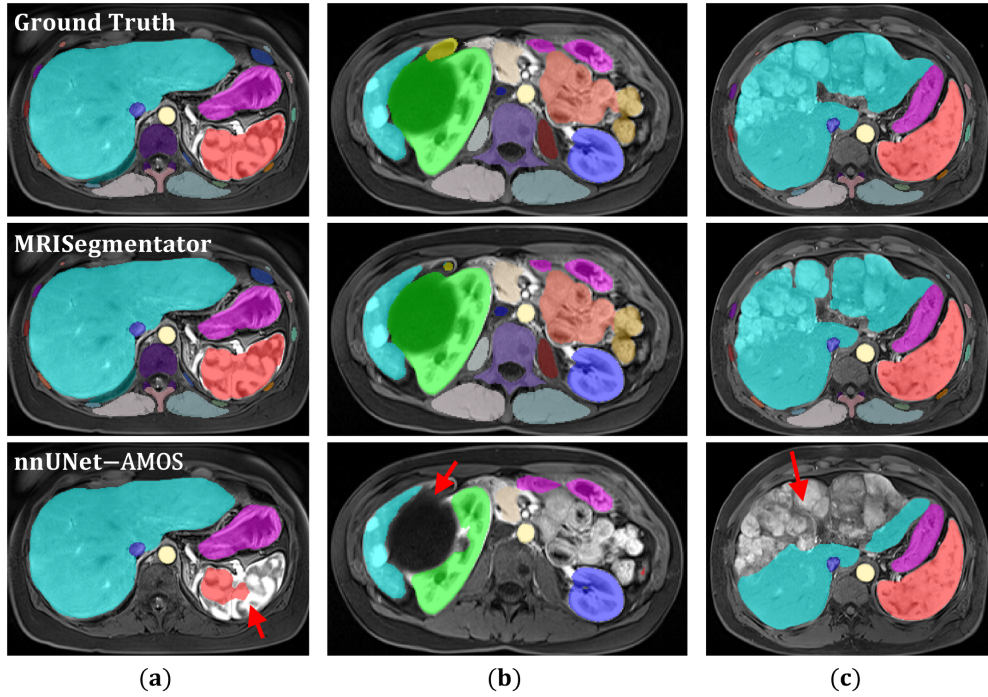


Fig. 6: Comparison of MRISegmentator and nnUNet-AMOS with ground truth on segmenting structures with different types of pathology. nnUNet-AMOS struggled to segment the same regions as highlighted by the red arrows in the last row. (a) shows a patient with heterogeneous splenic attenuation during the arterial phase of enhancement; (b) shows a patient with a hypo-intense kidney lesion; (c) shows multiple liver lesions in a patient with metastatic disease.

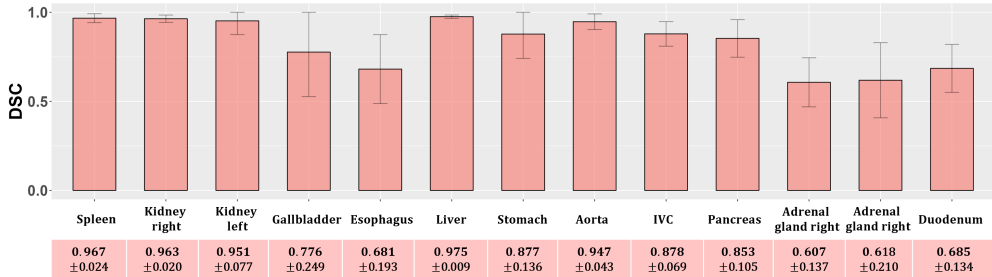


Fig. 7: The segmentation performance of MRISegmentator for 13 major organs in the train + validation subsets of the AMOS22 dataset.

On the Duke Liver dataset, the DSC scores for the PRE, ART, and VEN phases were 0.912 ± 0.055 , 0.946 ± 0.012 , 0.942 ± 0.019 , respectively. The NSD scores were 0.903 ± 0.070 , 0.929 ± 0.024 , and 0.956 ± 0.017 , respectively. MRISegmentator achieved

DSC scores of > 0.9 across all three sequences (PRE, ART, and VEN). The lowest DSC score was observed in the PRE sequence, attributable to the reduced contrast inherent in pre-contrast imaging.

5 Discussion

The proposed MRISegmentator is a multi-organ and structure segmentation tool that can automatically segment 62 abdominal organs and structures. MRISegmentator was extensively validated on an internal dataset and two external datasets from different institutions. Empirical results demonstrated that the model achieved average DSC scores of exceeding 0.90 for 15 major organs (except the adrenals glands), 7 blood vessels, and 8 muscles, and 0.80 for 35 bones. Furthermore, external validations showed its robust performance across two large abdominal MRI datasets from different institutions. MRISegmentator obtained an average DSC of 0.829 ± 0.133 for 13 organs in the AMOS22 dataset, and attained DSC scores of > 0.9 across all three sequences (PRE, ART, and VEN) in the external Duke Liver dataset.

The segmentation performance on the external AMOS22 dataset was not as high as the results observed in the internal dataset. MRISegmentator achieved a DSC score of ≥ 0.85 for the majority of organs, with the exception of several smaller organs such as the gallbladder, esophagus, adrenal glands, and duodenum. This discrepancy can be attributed to the non-T1w and non-axial volumes in the AMOS22 dataset². These series types were unseen during the training phase of MRISegmentator and diverged from the training data distribution. Nevertheless, MRISegmentator showed its robustness to different coronal volumes. Fig. 12 in the supplementary materials demonstrates the segmentation results of a patient in coronal-view T1w MRI from the AMOS22 dataset. On the validation set of the AMOS22 MRI subset (20 patients, 20 volumes), though MRISegmentator was not directly trained with the AMOS22 dataset, it still came in second when compared against other state-of-the-art methods that were trained directly on AMOS22 training set. This showcases the robust segmentation capabilities of MRISegmentator on a dataset obtained from an external institution.

Furthermore, the segmentation performance was sub-optimal for ribs and spinal vertebrae, particularly in the upper and lower abdomen near transitional zones of the chest and pelvis. Fig. 12 in the supplementary materials illustrates this issue. Results from the coronal volumes in the AMOS22 dataset contained a portion of the lower chest, and showed that parts of the lung, ribs, and spinal vertebrae were erroneously segmented. These errors occurred as the chest MRIs were not included in the training data. Chest MRI studies are infrequently acquired in our institution as patient motion from breathing can corrupt the MRI sequences.

To the best of our knowledge, multi-structure segmentation on the scale of our work has only been explored in a few recent studies. Chen *et al.* (Chen et al (2020)) proposed a 2D UNet-based method to segment 10 major abdominal organs and bones using their internal dataset of 102 patients, but this study covered only a limited number of structures. Ji *et al.* (Ji et al (2022)) provided the first publicly available MRI dataset

²Due to the absence of acquisition information in the AMOS22 dataset, excluding non-T1w images was challenging.

containing multi-structure labels as part of the AMOS22 challenge, and it featured annotations for 13 structures across 60 MRI volumes. However, the limited number of patients in this dataset posed significant challenges for model generalization, and lacked data acquisition parameters and patient demographic information. The Duke Liver dataset (Macdonald et al (2023)), while providing detailed sequence information, was primarily released for automated classification of MRI sequences and exclusively contains only liver segmentations. More recently, several concurrent works on multi-organ and structure segmentation for MRI have emerged. Gu *et al.* (Gu et al (2024)) proposed a universal bone segmentation network to segment skeletal structures in MRI. In parallel, Zhou *et al.* (Zhou et al (2024)) proposed MRAnnotator to segment 49 structures in the whole body. Geißler *et al.* (Geißler et al (2024)) proposed a TS-like tool for T1 Dixon MRI using global intensity non-linear data augmentation. However, these tools encompassed fewer structures in contrast to our work. In addition, the datasets or models were not publicly available. In our study, we have created a robust tool to segment 62 organs and structures, and it has been comprehensively evaluated.

There are some limitations to our study. First, the internal dataset included patients with a broad range of pathologies, and an analysis of this effect posed on the segmentation accuracy of MRISegmentator has not been evaluated. Second, this study solely focused on pre-contrast and dynamic contrast enhanced T1-weighted MRI series. Other MRI sequences, such as T1 Dixon MRI, T1 in-phase/opposed phase, T2-weighted and T2 Fat-Suppressed, were not considered and are the subject of future work. Additionally, the current work only focused on axially acquired series, but as described above, it was robust to coronal and sagittal sequences as well. Third, chest or pelvic MRI studies were not considered. The former is less frequently acquired and the latter is a potential avenue for future work (Zhuang et al (2024)). Fourth, we did not compare our 3D nnUNet model against other approaches, such as transformer-based segmentation models or foundation models. The nnUNet framework was robustly validated on a variety of segmentation challenges and it is the *de-facto* standard for medical segmentation tasks (Isensee et al (2024)). Finally, the testing set was reviewed by a single radiologist and inter-rater variability of segmentations was not performed.

In conclusion, a multi-parametric T1-weighted MRI segmentation tool called MRISegmentator that accurately and reliably segments 62 organs and structures in body MRI has been presented. The tool has the potential to be easily integrated into the clinical workflow for various tasks, such as abnormality detection, early detection of cancer, and opportunistic screening with body composition measurements among others. MRISegmentator is efficient and accurate, and it can save time when initial organ or structure segmentations are needed for downstream tasks, such as tracking interval changes in size.

Acknowledgments. This work was supported by the Intramural Research Program of the National Institutes of Health (NIH) Clinical Center (project number 1Z01 CL040004). This work used the computational resources of the NIH HPC Biowulf cluster.

Declarations. The authors declare the following financial interests/personal relationships which may be considered as potential competing interests: Ronald M.

Summers reports a relationship with Ping An (CRADA) that includes: funding grants. Co-author RMS receives royalties from iCAD, Philips, ScanMed, PingAn, MGB, and Translation Holdings.

References

- Billot B, Magdamo C, Cheng Y, et al (2023) Robust machine learning segmentation for large-scale analysis of heterogeneous clinical brain mri datasets. *Proceedings of the National Academy of Sciences* 120(9):e2216399120
- Chen Y, Ruan D, Xiao J, et al (2020) Fully automated multiorgan segmentation in abdominal magnetic resonance imaging with deep neural networks. *Medical physics* 47(10):4971–4982
- Dirix P, Haustermans K, Vandecaveye V (2014) The value of magnetic resonance imaging for radiotherapy planning. *Seminars in Radiation Oncology* 24(3):151–159. <https://doi.org/https://doi.org/10.1016/j.semradonc.2014.02.003>, URL <https://www.sciencedirect.com/science/article/pii/S1053429614000204>, magnetic Resonance Imaging in Radiation Oncology
- Geißler K, Mensing D, Wenzel M, et al (2024) Towards totalsegmentator for mri data leveraging gin data augmentation. *SPIE Medical Imaging 2024: Computer-Aided Diagnosis*
- Greenspan H, Van Ginneken B, Summers RM (2016) Guest editorial deep learning in medical imaging: Overview and future promise of an exciting new technique. *IEEE transactions on medical imaging* 35(5):1153–1159
- Gu H, Colglazier R, Dong H, et al (2024) Segmentanybone: A universal model that segments any bone at any location on mri. *arXiv preprint arXiv:240112974*
- Hatamizadeh A, Nath V, Tang Y, et al (2021) Swin unetr: Swin transformers for semantic segmentation of brain tumors in mri images. *International MICCAI Brainlesion Workshop* pp 272–284
- Hatamizadeh A, Tang Y, Nath V, et al (2022) Unetr: Transformers for 3d medical image segmentation. *2022 IEEE/CVF Winter Conference on Applications of Computer Vision (WACV)* pp 1748–1758
- Isensee F, Jaeger PF, Kohl SA, et al (2021) nnu-net: a self-configuring method for deep learning-based biomedical image segmentation. *Nature methods* 18(2):203–211
- Isensee F, Wald T, Ulrich C, et al (2024) nnu-net revisited: A call for rigorous validation in 3d medical image segmentation. *arXiv preprint arXiv:240409556*
- Ji Y, Bai H, Ge C, et al (2022) Amos: A large-scale abdominal multi-organ benchmark for versatile medical image segmentation. *Advances in Neural Information*

- Keall PJ, Brighi C, Glide-Hurst C, et al (2022) Integrated mri-guided radiotherapy—opportunities and challenges. *Nature Reviews Clinical Oncology* 19(7):458–470
- Ma J, Zhang Y, Gu S, et al (2022) Abdomenct-1k: Is abdominal organ segmentation a solved problem? *IEEE Transactions on Pattern Analysis and Machine Intelligence* 44(10):6695–6714. <https://doi.org/10.1109/TPAMI.2021.3100536>
- Macdonald JA, Zhu Z, Konkel B, et al (2023) Duke liver dataset: A publicly available liver mri dataset with liver segmentation masks and series labels. *Radiology: Artificial Intelligence* 5(5):e220275
- Mathai TS, Lee S, Elton DC, et al (2022) Lymph node detection in t2 mri with transformers. *SPIE Medical Imaging 2022: Computer-Aided Diagnosis* 12033:855–859
- Mathai TS, Lee S, Shen TC, et al (2023) Universal lymph node detection in t2 mri using neural networks. *International Journal of Computer Assisted Radiology and Surgery* 18(2):313–318
- Mathai TS, Shen TC, Elton DC, et al (2024) Detection of abdominopelvic lymph nodes in multi-parametric mri. *Computerized Medical Imaging and Graphics* p 102363
- Milletari F, Navab N, Ahmadi S (2016) V-net: Fully convolutional neural networks for volumetric medical image segmentation. 2016 Fourth International Conference on 3D Vision (3DV) pp 565–571
- Nyholm T, Svensson S, Andersson S, et al (2018) Mr and ct data with multiobserver delineations of organs in the pelvic area—part of the gold atlas project. *Medical physics* 45(3):1295–1300
- Park S, Chu L, Fishman E, et al (2020) Annotated normal ct data of the abdomen for deep learning: Challenges and strategies for implementation. *Diagnostic and interventional imaging* 101(1):35–44
- Ronneberger O, Fischer P, Brox T (2015) U-net: Convolutional networks for biomedical image segmentation. In: Navab N, Hornegger J, Wells WM, et al (eds) *Medical Image Computing and Computer-Assisted Intervention – MICCAI 2015*. Springer International Publishing, Cham, pp 234–241
- Wasserthal J, Breit HC, Meyer MT, et al (2023) Totalsegmentator: Robust segmentation of 104 anatomic structures in ct images. *Radiology: Artificial Intelligence* 5(5)

- Xie Y, Zhang J, Shen C, et al (2021) Cotr: Efficiently bridging cnn and transformer for 3d medical image segmentation. In: de Bruijne M, Cattin PC, Cotin S, et al (eds) Medical Image Computing and Computer Assisted Intervention – MICCAI 2021. Springer International Publishing, Cham, pp 171–180
- Zaffina C, Wyttenbach R, Pagnamenta A, et al (2022) Body composition assessment: Comparison of quantitative values between magnetic resonance imaging and computed tomography. *Quantitative imaging in medicine and surgery* 12(2):1450
- Zhou A, Liu Z, Tieu A, et al (2024) Mrannotator: A multi-anatomy deep learning model for mri segmentation. arXiv preprint arXiv:240201031
- Zhou HY, Guo J, Zhang Y, et al (2021) nnformer: Interleaved transformer for volumetric segmentation. arXiv preprint arXiv:210903201
- Zhu Q, Mathai TS, Mukherjee P, et al (2023) Utilizing longitudinal chest x-rays and reports to pre-fill radiology reports. arXiv preprint arXiv:230608749
- Zhuang X, Li L, Payer C, et al (2019) Evaluation of algorithms for multi-modality whole heart segmentation: an open-access grand challenge. *Medical image analysis* 58:101537
- Zhuang Y, Mathai TS, Mukherjee P, et al (2024) Segmentation of pelvic structures in t2 mri via mr-to-ct synthesis. *Computerized Medical Imaging and Graphics* p 102335

6 Supplemental Materials

6.1 The internal dataset

Fig. 8 shows the STARD chart detailing the inclusion and exclusion criteria for the internal dataset. Table 1 shows a summary of the acquisition information for the internal dataset.

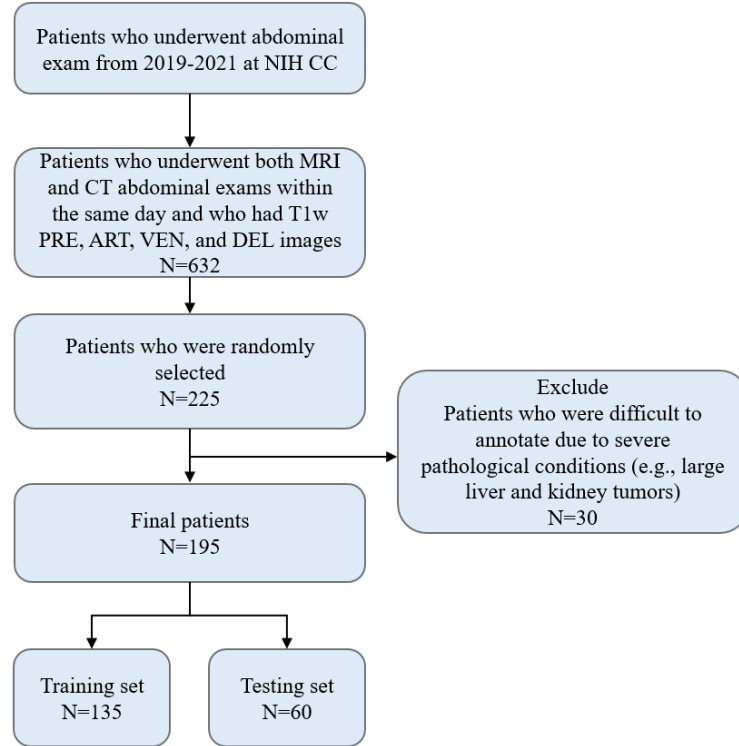


Fig. 8: The Standards for Reporting of Diagnostic Accuracy (STARD) chart that details the inclusion and exclusion criteria for the internal dataset.

6.2 The Duke Liver dataset

Fig. 9 shows the STARD chart detailing the inclusion and exclusion criteria for the external Duke Liver dataset used in this study. Table 2 shows a summary of the acquisition parameters and demographics information for the external Duke Liver dataset.

Table 1: Details on the MRI acquisition and patient demographics for the internal T1-weighted MRI dataset.

Internal Dataset		
Acquisition information (T1w PRE, ART, VEN, DEL)		
	Train	Test
Number of volumes (patients)	540 (135)	240 (60)
Width range	228-320	320-320
Height range	240-320	220-290
Number of slices	80-96	80-104
Slice thickness range (mm)	3.0-3.3	3
Pixel spacing range (mm)	(0.937-1.468)x(0.937-1.468)	(1.0-1.375)x(1.0-1.375)
TR (msec)	3.65-3.88	3.65-3.81
TE (msec)	1.67-1.92	1.69-1.87
Flip Angle	10	10
Field strength	1.5, 3	1.5, 3
Demographics information		
	Train	Test
Age, mean±std	54.67±16.27	51.12±14.39
min, max	16, 87	23, 83
Gender ratio (female: male)	72:63	26:34
White	100	53
Black	13	1
Asian	10	2
Native Americans	1	0
Native Hawaiian or other pacific islander	1	0
Multiracial	4	1
Unknown	6	3

Table 2: Acquisition and demographics information for the subset of the Duke Liver Dataset used in our study

Duke Liver Dataset			
Acquisition information (T1w PRE, ART, VEN)		Demographics information	
Number of series (patients)	177 (95)	Age, mean±std	55.66±20.68
Width range	256-576	Age, min, max	3, 79
Height range	256-576	Gender ratio	27:65
Number of slices	44-168	White	-
Slice thickness range (mm)	3.0-7.0	African American	-
Pixel spacing range (mm)	(0.683-1.679)x(0.683-1.679)	Asian	-
TR (msec)	3.66-7.49	Native American	-
TE (msec)	1.07-3.12	Native Hawaiian or other pacific islander	-
Flip Angle	9-12	Multiracial	-
Field strength	1.5, 3	unknow	-

6.3 The acquisition information for the internal CT dataset

Table 3 shows a summary of the acquisition information for the internal CT dataset used for the annotation.

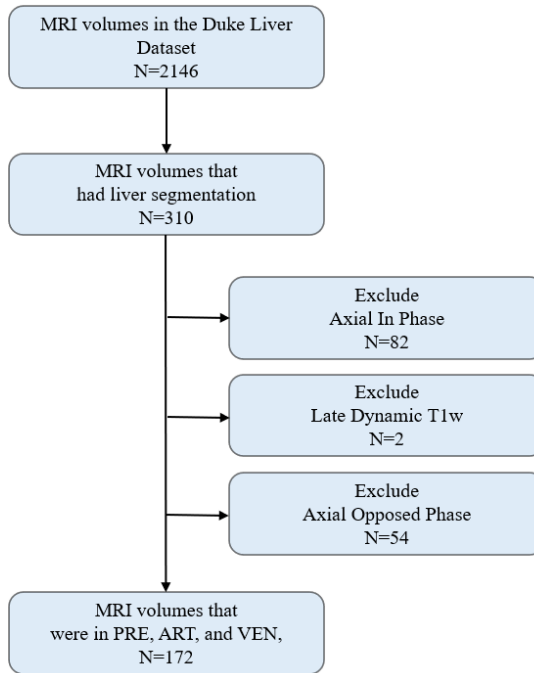


Fig. 9: The STARD chart detailing the inclusion and exclusion criteria for the external Duke Liver dataset.

Table 3: The acquisition information for the CT data.

Scanner	Manufacture	Width range	Height range	Number of slices	Pixel spacing range (mm)	Slice thickness range (mm)
Biograph128/SOMATOM_Force	Siemens	512	512	47-806	0.675 - 0.976	1.0-5.0

6.4 MRISegmentator - 62 abdominal organs and structures

The list below enumerates the 62 main organs and structures of interest, divided into 4 different groups based on their anatomical locations and physiology:

- **Group 1 (G1)** includes 15 main organs and structures in the abdomen: spleen, kidney_right, kidney_left, gallbladder, liver, esophagus, stomach, pancreas, adrenal gland_right, adrenal gland_left, duodenum, lung_right, lung_left, small bowel, colon.
- **Group 2 (G2)** includes 7 vessels: aorta, inferior vein cava, portal vein and splenic vein, iliac artery_left, iliac artery_right, iliac vein_left, iliac vein_right.
- **Group 3 (G3)** includes 8 muscles: gluteus maximus_left, gluteus maximus_right, gluteus medius_left, gluteus medius_right, autochthon_left, autochthon_right, iliopsoas_left, iliopsoas_right.
- **Group 4 (G4)** includes 32 bones: hip_left, hip_right, sacrum, rib_left_4, rib_left_5, rib_left_6, rib_left_7, rib_left_8, rib_left_9, rib_left_10, rib_left_11, rib_left_12, rib_right_4, rib_right_5, rib_right_6, rib_right_7, rib_right_8, rib_right_9, rib_right_10,

rib_right_11, rib_right_12, vertebrae_T7, vertebrae_T8, vertebrae_T9, vertebrae_T10, vertebrae_T11, vertebrae_T12, vertebrae_L1, vertebrae_L2, vertebrae_L3, vertebrae_L4, vertebrae_L5.

6.5 Tabular results

Tables 4 and 5 detail the Dice Similarity Coefficient (DSC) and Normalized Surface Distance (NSD) obtained by MRISegmentator for all the 62 organs and structures in the internal dataset.

Table 6 shows DSC and NSD comparison results for MRISegmentator and nnUNet-AMOS on the internal dataset, and MRISegmentator’s performance on the AMOS22 dataset.

Table 4: MRISegmentator - DSC of 62 organs and structures in abdomen.

	Organ & structure	DSC(mean±std)	Organ & structure	DSC(mean±std)	Organ & structure	DSC(mean±std)	Organ & structure	DSC(mean±std)		
	spleen	0.977±0.015	aorta	0.990±0.006	hip_left	0.936±0.121	rib_left_6	0.848±0.249		
	lung_left	0.976±0.009	inferior_vein_cava	0.974±0.019	hip_right	0.917±0.113	rib_left_7	0.782±0.258		
	lung_right	0.984±0.006	portal_vein_and_splenic_vein	0.777±0.239	sacrum	0.806±0.245	rib_left_8	0.834±0.215		
	kidney_right	0.984±0.010	iliac_artery_right	0.931±0.075	vertebrae_T7	0.682±0.307	rib_left_9	0.846±0.234		
	kidney_left	0.970±0.093	iliac_artery_left	0.904±0.153	vertebrae_T8	0.833±0.270	rib_left_10	0.848±0.249		
	gallbladder	0.918±0.109	iliac_vein_left	0.909±0.123	vertebrae_T9	0.874±0.247	rib_left_11	0.836±0.253		
	liver	0.993±0.002	iliac_vein_right	0.908±0.118	vertebrae_T10	0.905±0.230	rib_left_12	0.783±0.286		
	esophagus	0.915±0.107	glutens_medius_right	0.924±0.132	vertebrae_T11	0.914±0.222	rib_right_4	0.482±0.353		
G1	stomach	0.965±0.044	glutens_medius_left	0.827±0.239	G4	vertebrae_T12	0.915±0.229	G4	rib_right_5	0.626±0.336
	pancreas	0.931±0.080	glutens_maximus_left	0.827±0.239	vertebrae_L1	0.915±0.216	rib_right_6	0.707±0.311		
	adrenal_gland_right	0.669±0.203	glutens_maximus_right	0.771±0.278	vertebrae_L2	0.933±0.157	rib_right_7	0.762±0.286		
	adrenal_gland_left	0.653±0.217	autochthon_left	0.992±0.001	vertebrae_L3	0.931±0.182	rib_right_8	0.811±0.245		
	duodenum	0.898±0.073	autochthon_right	0.991±0.002	vertebrae_L4	0.915±0.213	rib_right_9	0.825±0.223		
	small_bowel	0.968±0.036	iliopsoas_right	0.987±0.004	vertebrae_L5	0.854±0.256	rib_right_10	0.820±0.232		
	colon	0.965±0.032	iliopsoas_left	0.981±0.049	rib_left_4	0.516±0.365	rib_right_11	0.807±0.223		
	-	-	-	-	rib_left_5	0.660±0.337	rib_right_12	0.788±0.277		

Table 5: NSD results of the proposed MRISegmentator tool for 62 organs and structures in the internal dataset.

	Organ & structure	NSD(mean±std)	Organ & structure	NSD(mean±std)	Organ & structure	NSD(mean±std)	Organ & structure	NSD(mean±std)		
	spleen	0.982±0.019	aorta	0.999±0.003	hip_left	0.980±0.112	rib_left_6	0.824±0.298		
	lung_left	0.974±0.017	inferior_vein_cava	0.996±0.014	hip_right	0.987±0.075	rib_left_7	0.870±0.247		
	lung_right	0.990±0.010	portal_vein_and_splenic_vein	0.879±0.228	sacrum	0.912±0.224	rib_left_8	0.910±0.215		
	kidney_right	0.988±0.015	iliac_artery_right	0.989±0.033	vertebrae_T7	0.841±0.317	rib_left_9	0.913±0.232		
	kidney_left	0.968±0.091	iliac_artery_left	0.967±0.142	vertebrae_T8	0.907±0.244	rib_left_10	0.910±0.248		
	gallbladder	0.966±0.069	iliac_vein_left	0.987±0.081	vertebrae_T9	0.928±0.225	rib_left_11	0.903±0.251		
	liver	0.993±0.009	iliac_vein_right	0.986±0.058	vertebrae_T10	0.935±0.212	rib_left_12	0.884±0.277		
	esophagus	0.971±0.062	glutens_medius_right	0.968±0.110	vertebrae_T11	0.940±0.204	rib_right_4	0.658±0.413		
G1	stomach	0.963±0.063	glutens_medius_left	0.997±0.014	G4	vertebrae_T12	0.936±0.219	G4	rib_right_5	0.771±0.348
	pancreas	0.962±0.080	glutens_maximus_left	0.921±0.251	vertebrae_L1	0.942±0.190	rib_right_6	0.817±0.315		
	adrenal_gland_right	0.879±0.212	glutens_maximus_right	0.893±0.243	vertebrae_L2	0.955±0.142	rib_right_7	0.845±0.288		
	adrenal_gland_left	0.846±0.235	autochthon_left	0.999±0.001	vertebrae_L3	0.957±0.169	rib_right_8	0.887±0.240		
	duodenum	0.942±0.065	autochthon_right	0.999±0.001	vertebrae_L4	0.944±0.197	rib_right_9	0.906±0.227		
	small_bowel	0.978±0.030	iliopsoas_right	0.996±0.013	vertebrae_L5	0.923±0.217	rib_right_10	0.906±0.241		
	colon	0.977±0.032	iliopsoas_left	0.992±0.043	rib_left_4	0.672±0.442	rib_right_11	0.905±0.223		
	-	-	-	-	rib_left_5	0.795±0.340	rib_right_12	0.893±0.249		

Table 6: DSC and NSD results of MRISegmentator and nnUNet-AMOS on the internal dataset, and the validation subset of the external AMOS22 dataset.

	The internal dataset				The AMOS22 dataset	
	MRISegmentator		nnUnet-AMOS		MRISegmentator	
	DSC	NSD	DSC	NSD	DSC	NSD
Spleen	0.977±0.015	0.982±0.019	0.939±0.131	0.931±0.139	0.967±0.024	0.981±0.034
Kidney_right	0.984±0.010	0.988±0.015	0.967±0.091	0.979±0.028	0.963±0.020	0.974±0.027
Kidney_left	0.970±0.093	0.968±0.091	0.962±0.114	0.947±0.118	0.951±0.077	0.966±0.069
Gallbladder	0.918±0.109	0.969±0.069	0.779±0.283	0.852±0.264	0.776±0.249	0.827±0.264
Esophagus	0.915±0.107	0.971±0.062	0.815±0.148	0.955±0.077	0.681±0.193	0.866±0.180
Liver	0.993±0.002	0.993±0.009	0.984±0.019	0.982±0.031	0.975±0.009	0.966±0.024
Stomach	0.965±0.044	0.963±0.063	0.837±0.199	0.855±0.190	0.877±0.136	0.879±0.143
Aorta	0.990±0.006	0.999±0.003	0.960±0.031	0.990±0.022	0.947±0.043	0.991±0.032
IVC	0.974±0.019	0.996±0.014	0.902±0.070	0.954±0.070	0.878±0.069	0.959±0.055
Pancreas	0.931±0.080	0.962±0.080	0.841±0.174	0.896±0.167	0.853±0.105	0.913±0.112
Adrenal_gland_right	0.669±0.203	0.879±0.212	0.544±0.231	0.765±0.251	0.607±0.137	0.886±0.105
Adrenal_gland_left	0.653±0.217	0.846±0.235	0.458±0.257	0.660±0.306	0.618±0.210	0.820±0.242
Duodenum	0.898±0.073	0.942±0.065	0.774±0.156	0.849±0.142	0.685±0.134	0.783±0.143

6.6 Example segmentation results of patients from the AMOS22 dataset and Duke Liver dataset

Figs. 10 and 11 show the segmentation results for the AMOS22 and Duke Liver datasets.

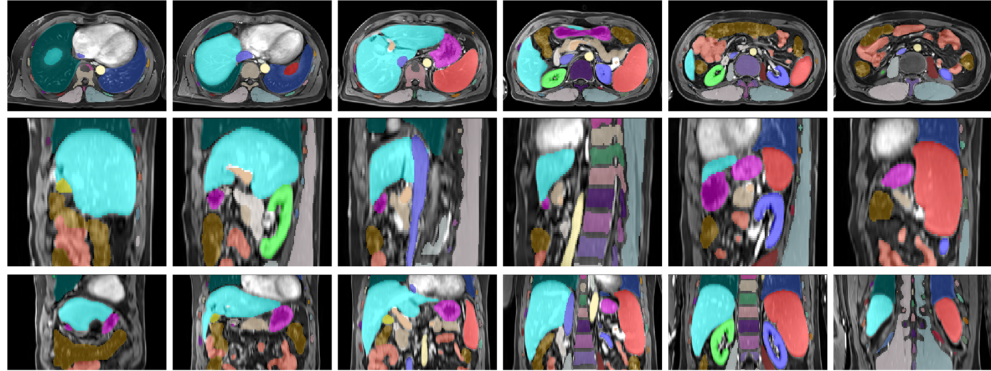


Fig. 10: Segmentation results of one patient from the AMOS dataset. Top, middle, and bottom rows show axial, sagittal, and coronal views.

6.7 Color map of the segmentation mask

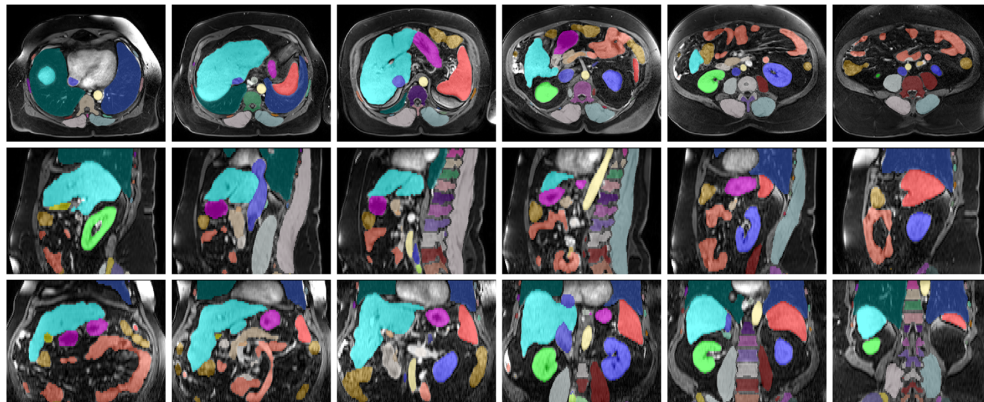


Fig. 11: Segmentation results of one patient from the Duke Liver dataset. Top, middle, and bottom rows show axial, sagittal, and coronal views.

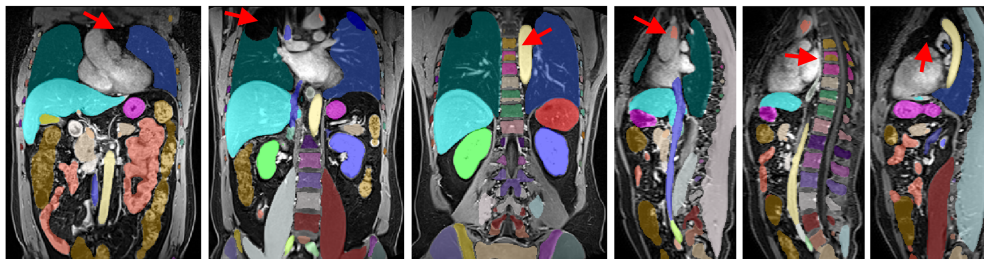


Fig. 12: Segmentation results of a patient in coronal-view T1w MRI from the AMOS22 dataset. The red arrows indicated the segmentation errors in the chest.



Fig. 13: The color map of the segmentation masks for the 62 organs and structures used for visualization.